

1 **Cornelia-de Lange syndrome-associated mutations cause a DNA damage**
2 **signalling and repair defect**

3
4 Gabrielle Olley¹, Madapura M. Pradeepa^{1,2}, David R. FitzPatrick¹, Wendy A. Bickmore*¹ Charlene
5 Boumendil*¹
6

7 ¹MRC Human Genetics Unit, Institute of Genetics and Molecular Medicine, University of Edinburgh,
8 Crewe Road, Edinburgh EH4 2XU, UK
9

10 ² Blizard institute, Barts and The London School of Medicine and Dentistry, Queen Mary
11 University of London, London, E1 2AT
12

13 *Correspondence to:

14 W.A.B or C.B: MRC Human Genetics Unit, IGMM, Crewe Road, Edinburgh EH4 2XU, UK

15 Tel: +44 131 651 8570

16 Email: Wendy.Bickmore@igmm.ed.ac.uk, Charlene.Lemaitre@igmm.ed.ac.uk
17

18 Running title: BRD4, DNA damage and disease
19
20
21
22
23
24
25
26
27
28
29
30
31
32
33
34
35
36
37
38
39
40
41
42
43
44
45
46
47
48

49 **Summary**

50

51 Cornelia de Lange Syndrome is a multisystem developmental disorder typically caused by mutations in
52 the gene encoding the cohesin loader NIPBL. The associated phenotype is generally assumed to be
53 the consequence of aberrant transcriptional regulation. Recently, we identified a residue substitution in
54 BRD4 associated with a Cornelia de Lange-like syndrome, that reduces BRD4 binding to acetylated
55 histones. Here we show that, although this mutation reduces BRD4-occupancy at enhancers in mouse
56 embryonic stem cells, it does not affect transcription. Rather it delays the cell cycle, increases DNA
57 damage signalling, and perturbs regulation of DNA repair in mutant cells. This uncovers a new role for
58 BRD4 in DNA repair pathway choice. Furthermore, we find evidence of a similar increase in DNA
59 damage signalling in cells derived from NIPBL-deficient individuals, suggesting that defective DNA
60 damage signalling and repair is also a feature of typical Cornelia de Lange Syndrome.

61

62 **Introduction**

63 Cornelia de Lange Syndrome (CdLS) is a clinically distinctive neurodevelopmental disorder
64 (OMIM:122470). Disease severity varies greatly and patients can suffer from a range of symptoms
65 including: a characteristic facial appearance, upper limb abnormalities, intellectual disability and
66 delayed growth¹. CdLS is described as a 'cohesinopathy'¹ - most cases can be attributed to
67 heterozygous loss of function mutation in *NIPBL* encoding a protein involved in loading of the cohesin
68 complex onto chromatin². Mutation in genes encoding cohesin complex proteins *SMC1*, *SMC3* and
69 *RAD21*, or *HDAC8* (*SMC3* deacetylase), have also been identified in CdLS-like probands². However
70 cells from CdLS patients have no obvious defects in sister chromatid cohesion³, and individuals with
71 mutations in *SMC1*, *SMC3* and *RAD21* are often considered 'atypical' in terms of facial appearance and
72 growth, and are less likely to have limb defects than those with *NIPBL* mutations⁴.

73 Dysregulated gene expression has been proposed to be main mechanism underlying CDLS^{5,6}.
74 Mutations in genes encoding chromatin regulators unrelated to cohesin, such as *ANKRD11*, *KMT2A*,
75 *AFF4* and the bromodomain and extra-terminal domain (BET) protein *BRD4*, have been reported to
76 cause CdLS-like phenotypes¹ suggesting that chromatin dysregulation may play a role in CdLS as well.
77 Additionally, increased sensitivity to DNA damage has been reported in CdLS patient cells⁷, but the
78 mechanism underlying this defect is unknown and its participation in the disease aetiology remains
79 unclear.

80 Recently, we described *de novo* deletion and missense mutations in *BRD4* associated with a clinical
81 phenotype overlapping CdLS⁸. *BRD4* binds acetylated lysines residues in histones H3 and H4 through
82 its two N-terminal bromodomain domains (BD). *BRD4* localises to promoters and enhancers of active
83 genes and is particularly enriched at super enhancers (SEs)^{9,10}. *BRD4* is a key regulator of transcription;
84 through its C-terminal domain it recruits positive transcription elongation factor (P-TEFb) and the
85 Mediator complex to promoters and enhancers, whilst its extra-terminal domain confers transcriptional
86 activation through the recruitment of *CHD4*, *JMJD6*, and *NSD3*^{11,12}.

87 The CdLS-associated BRD4 missense mutation is in the second bromodomain (BD2)
88 (NM_058243.2:c.1289A>G, p.(Tyr430Cys), termed here as Y430C (Figure 1A), and results in
89 decreased binding to acetylated histones⁸. To gain further insights into the mechanisms underlying
90 CdLS, and the role of BRD4, we investigated the phenotype of mouse embryonic stem cells (mESCs)
91 homozygous for the orthologous amino acid substitution in mouse Brd4 (actually p.Tyr431Cys but for
92 simplicity here termed *Brd4*^{Y430C}). Here we show that the decreased affinity for acetylated lysines results
93 in diminished occupancy of BRD4^{Y430C} at cis regulatory elements (CREs) across the genome. However,
94 we find no evidence of altered transcription in these cells. Instead, we report increased and more
95 persistent DNA damage signaling and cell cycle checkpoint activation in *Brd4*^{Y430C} mESCs. We show
96 increased persistent foci of the DNA damage response (DDR) protein 53BP1 upon double-strand break
97 (DSB) induction in Brd4 mutant cells. 53BP1 is a key factor in the regulation of DNA repair pathway
98 choice that inhibits repair by homologous recombination (HR). We also show increased foci of the
99 downstream effectors of 53BP1, Rif1 and the Mad2l2 (Rev7) subunit of the shieldin complex in the
100 mutant cells^{13–22} and decreased recruitment of RAD51, suggesting impaired HR repair. Further, we
101 show that cells from CdLS patients harbouring mutations in *NIPBL* have a similar DDR phenotype,
102 indicating there may be a previously underappreciated role for the DNA damage response in the
103 aetiology of CdLS.

104

105 **Results**

106

107 **Reduced occupancy of Y430C-BRD4 at cis-regulatory elements**

108 Our previous work suggested that the Y430C mutation abrogates BRD4 binding to acetylated histones
109 *in vitro* and *in vivo*⁸. To determine the genome-wide effect of this loss of affinity we carried out BRD4
110 ChIP-seq in two independently-generated mESCs lines engineered by CRISPR-Cas9 to carry the
111 Y430C mutation on both alleles of *Brd4*. As expected, BRD4 was enriched over CREs (SEs, typical
112 enhancers and promoters) in both wild-type (WT) and Y430C cells (Figure 1B, Supplementary figure
113 1A). However, consistent with a decreased affinity for acetyl-lysines, there was a general decrease in
114 BRD4 occupancy in Y430C cells, most striking at enhancers and super-enhancers (SE) (Figure 1C,D,
115 Supplementary figure S1A-C). Nevertheless, Y430C binding was still sensitive to further perturbation
116 by the BET inhibitor JQ1 (Supplementary figure 1C). In mESCs, BRD4 binding to SEs regulates the
117 transcription of stem cell identity genes⁹. As BRD4^{Y430C} occupancy is decreased at the SEs of a number
118 of stem cell identity genes, this suggests that there might be decreased transcription of these genes in
119 mutant cells.

120

121 **Decreased BRD4 at CREs does not affect transcription**

122 The use of inhibitors that competitively bind the acetyl-lysine binding pockets of BET proteins has shown
123 that loss of BRD4 binding disrupts the expression of target genes, especially genes regulated by SEs
124 ¹⁰. Consistent with this, we observed decreased expression of the SE associated genes *Nanog*, *Myc*,

125 *Klf4* and *Oct4* in WT mESCs after treatment with JQ1 (Figure 2A). However, we did not observe any
126 decrease in levels of *Klf4*, *Nanog* and *Oct4* mRNAs in Y430C cells by RT-qPCR (Figure 2B).

127 To determine whether mRNA stability was masking an effect on transcription per se, we performed 4-
128 thiouridine sequencing (4SU-seq) to assay nascent transcription. Transcription was surprisingly similar
129 between WT and Y430C mESCs (Pearson correlation coefficient=0.98) (Figure 2C,D and
130 Supplementary figure 2A). In particular, decreased BRD4 binding at SEs did not lead to transcriptional
131 changes at stem cell identity genes (Figure 2C-E, Supplementary figure 2B), or of eRNAs at the SEs
132 themselves (Figure 2F, Supplementary figure 2C). Due to normalization, these experiments could not
133 rule out that transcription is not globally decreased in the mutant cells. We therefore performed a spike-
134 in RNA-seq experiment, using RNA from *Drosophila* cells for normalization. Again, we did not observe
135 any major transcriptional differences between WT and Y430C cells (Supplementary figure 2D&E). We
136 conclude that the decreased occupancy of BRD4^{Y430C} at CREs in mESCs is not sufficient to affect the
137 transcription of associated genes. This result is surprising, given BRD4's well documented roles in
138 transcriptional regulation.

139

140 **Y430C-BRD4 mESCs have a delayed cell cycle and increased cell cycle checkpoint activation**

141 We noted that BRD4^{Y430C} mESCs grew slower, and showed an accumulation of cells in G2/M (33.7%),
142 compared to their WT counterparts (27.8%) (Figure 3A, B, Supplementary Figure 3A). This observation,
143 together with the recently reported roles for BRD4 in the DDR and DNA repair²³⁻²⁶ led us to investigate
144 potential DDR defects in mutant cells.

145 The DDR allows coordination between DNA repair and cell cycle progression. Recognition of DNA
146 damage by sensor proteins initiates a cascade that results in the phosphorylation and activation of the
147 checkpoint kinases CHK1 and CHK2, delaying or blocking cell cycle progression²⁷. CHK1 is the main
148 kinase required for delay at G2/M²⁷. To determine whether the altered cell cycle in BRD4^{Y430C} cells is
149 associated with increased activation of the G2/M checkpoint, we analysed CHK1 phosphorylation
150 (CHK1-P) after treatment with neocarzinostatin (NCS), a radiomimetic drug which induces mainly DSBs.
151 CHK1-P is increased in both WT and BRD4^{Y430C} mESCs cell lines 1hr post NCS treatment, which is
152 resolved by 16hrs. However, the levels of CHK1-P are higher in BRD4^{Y430C} mESCs, suggesting an
153 increased checkpoint activation (Figure 3C). There is a similar increase in CHK1-P at intermediate (2,
154 4, 6 and 10hr post NCS) time points discounting the possibility that checkpoint activation simply occurs
155 faster in the mutant cells (Supplementary figure 3B).

156 These results suggest a defect in DNA repair or signaling caused by BRD4^{Y430C}. BRD4 has been shown
157 to be directly involved in DNA repair through the transcriptional regulation of DNA repair proteins^{24,25,28}.
158 However, 4SU-seq showed that transcription of genes encoding DNA repair proteins was unaffected in
159 BRD4^{Y430C} mESCs (Supplementary figure 3C, D).

160

161 **Y430C-BRD4 mESCs have increased DDR signalling**

162 BRD4 restricts the DDR and depletion of BRD4 isoform B leads to increased DDR signalling²³. We
163 therefore tested whether BRD4^{Y430C} affects DNA damage signalling. mESCs have constitutively high
164 levels of γ H2AX, even in the absence of a DNA damaging stimulus²⁹. We therefore used 53BP1 as a

165 marker of DDR. 53BP1 is recruited to DSBs, spreads to form microscopically visible foci, and acts as a
166 scaffold for the recruitment of further DSB response proteins, to regulate the choice of DNA repair
167 pathway and to promote cell cycle checkpoint signalling³⁰.

168 Immunofluorescence showed formation of multiple 53BP1 foci, representing DNA damage sites upon
169 DSB induction (1h after NCS treatment). These foci are only present at low levels prior to NCS treatment
170 and decrease in number at 16 and 20h post treatment, as cells repair the damage (Figure 4A).
171 Supporting the hypothesis that the Y430C mutation impairs the role of BRD4 in DDR restriction,
172 we observed that 53BP1 foci are larger in *BRD4*^{Y430C} mESCs than in WT (Figure 4A&B). In addition,
173 whilst the number of 53BP1 foci in WT cells returns to pre-treatment levels at 16 and 20h time points,
174 the number of 53BP1 foci in *BRD4*^{Y430C} cells remains higher (Figure 4A&C, Supplementary figure
175 4A&B), suggesting that DNA repair itself could be impaired.

176

177 **Defective DSB repair in Y430C-BRD4 cells**

178 For the most part, DSBs are repaired by either non-homologous end-joining (NHEJ) or HR³¹. Use of the
179 appropriate pathway is important for faithful repair and is determined by antagonistic recruitment of
180 53BP1 and BRCA1³⁰. 53BP1 inhibits DSB end resection, the initial step of HR, thereby promoting NHEJ
181 and inhibiting HR. Downstream effectors of 53BP1 in the regulation of resection include RIF1¹⁹⁻²² and
182 the recently identified shieldin complex (SHLD1, SHLD2, SHLD3 and MAD2L2)¹³⁻¹⁸. If timely repair
183 does not occur by NHEJ, BRCA1 promotes the release of RIF1, leading to end-resection and HR.

184 As *BRD4*^{Y430C} mESCs show increased numbers and size of 53BP1 foci compared to WT cells, we
185 reasoned that there may also be increased recruitment of the downstream effectors of 53BP1 such as
186 RIF1 and MAD2L2. Indeed, we observed an increased number of RIF1 (Figure 5A&B, Supplementary
187 figure 4C&D) and MAD2L2 (Figure 5C&D, Supplementary figure 4E&F) foci in *BRD4*^{Y430C} compared to
188 WT cells at all time-points, similar to the 53BP1. Conversely, we observed a significant decrease in the
189 number of foci of RAD51, a protein necessary for HR repair, in mutant cells at 1 hour post NCS (Figure
190 6A&B, Supplementary figure 4G&H), strongly suggesting a repression of HR. Given the role of the
191 shieldin complex in protecting DSB end-resection, we propose that the Y430C BRD4 mutation leads to
192 an altered balance between NHEJ and HR, consistent with the synthetic lethality observed between
193 BRD4 and PARP inhibitors^{25,28}.

194

195 **Increased number and size of 53BP1 foci in NIPBL mutation positive lymphoblastoid cell lines**

196 To see if the DDR defect that we have observed in the presence of the *BRD4*^{Y430C} would also be
197 apparent in cells carrying other CdLS mutations, we utilised two lymphoblastoid cell lines (LCL)
198 previously derived from CdLS patients with heterozygous mutations in NIPBL, Ile1206del³² and
199 Arg2298His³³. These LCLs have significantly more, and larger, 53BP1 foci per cell compared to a WT
200 LCL, in the absence of any exogenous damage (Figure 6C-E, Supplementary figure 5A&B). This
201 suggests that increased DDR signalling could be common to CdLS cases caused by BRD4 and NIPBL
202 mutations and that impaired DNA repair pathway choice balance may be a common mechanism
203 underlying CdLS.

204

205

206

207 **Discussion**

208 We previously showed that a Y430C-BRD4 mutation, and BRD4 haploinsufficiency, cause a CdLS-like
209 syndrome⁸. Previous studies have suggested that the severe developmental phenotypes associated
210 with CdLS are due to aberrant gene regulation. Here however, we show that BRD4^{Y430C}, whilst lowering
211 the affinity of BRD4 to acetylated lysine residues and decreasing its occupancy at enhancers and SEs,
212 causes minimal changes in transcription, at least in mESCs, in contrast to the transcriptional changes
213 caused by the profound loss of BRD4 binding induced by BET inhibitors. Instead, we provide evidence
214 that BRD4^{Y430C} causes increased G2/M checkpoint activation, aberrant DDR signalling, and an altered
215 focal accumulation of proteins that promote NHEJ and inhibit HR – 53BP1 and the shieldin complex.
216 Conversely there is a depletion of foci containing HR proteins (Rad51), suggesting a defect in HR. Our
217 results highlight a new role for BRD4 in the regulation of DNA repair pathway choice. Whether BRD4
218 mutation affects repair by HR at specific regions in the genome, or globally, remains to be investigated.
219 For example, different levels of histone acetylation in different chromatin environments – e.g.
220 heterochromatin vs euchromatin - upon DNA damage may recruit different amounts of BRD4^{34,35}.

221 Could aberrant DDR and DNA repair choice account for some of the phenotypes associated with CdLS?
222 Congenital mutation in genes involved in many different genes involved in cell cycle progression and
223 DNA repair, are - like CdLS – generally associated with intrauterine growth retardation and short
224 stature³⁶. Similarly, microcephaly also results from mutation in genes associated with S phase
225 progression (ATR, ATRIP1, RBBP8 - Seckl syndrome; DNA ligase IV – lig4 syndrome; XRCC4 –
226 microcephalic primordial dwarfism³⁷⁻³⁹). Clinically, there is strongest phenotypic overlap between CdLS
227 and Rubinstein-Taybi syndromes (RTS)- including arched eyebrows and other shared distinctive facial
228 features. RTS is caused by mutations in p300 or CREBBP. These lysine acetyltransferases have recently
229 been shown to be important for acetylating proteins involved in the DDR and DNA repair⁴⁰. NIPBL and
230 cohesin are also both involved in DNA damage signalling and repair⁴¹ and CdLS patient cells carrying
231 *NIPBL* mutations display an increased DNA damage sensitivity⁷. Furthermore, we show an increase in
232 53BP1 foci number and size, similar to that seen in *BRD4*^{Y430C} mESCs, in *NIPBL* haploinsufficient LCLs.
233 Even though we cannot discount that *BRD4* mutation in CdLS cases – Y430C, or heterozygous
234 deletions, cause aberrant transcriptional regulation in cell types other than ESCs, our results suggest
235 that dysregulation of DDR and repair may contribute to the aetiology of CdLS.

236

237

238 **Acknowledgments**

239 We thank the individuals with CdLS and their families for generously donating their samples and genetic
240 information and for consenting to their use in research studies. We thank Tom Strachan (Newcastle)
241 and Matt Deardorff and Ian Krantz (Children's Hospital of Philadelphia) for their gifts of CdLS LCLs. We
242 thank the Institute of Genetics and Molecular Medicine Advanced Imaging Resource for assistance with
243 imaging and Ilya Fliamer for his help with deposition of data on GEO. We thank Andrew Jackson (IGMM,
244 Edinburgh) for feedback on the manuscript.

245 G.O was supported by a PhD studentship from the Medical Research Council (MRC). M.M.P. is
246 supported by is supported by the Wellcome Trust Research seed award and funding from the School
247 of Medicine and Dentistry, QMUL. D.R.F is supported by MRC University Unit grant (MC_UU_00007/3)
248 and by the Simons Initiative for the Developing Brain. W.A.B is supported by MRC University Unit grant
249 (MC_UU_00007/2). C.B was supported by a H2020 Marie-Curie Individual Fellowship (655350-
250 NPCChr) and a Bettencourt-Schueller foundation prize for young researchers.

251 Authors contributions: W.A.B, P.M.M and C.B conceived and designed the experiments with input from
252 D.R.F. G.O conducted most of the experiments with help from P.M.M for ChIPseq and RNAseq
253 experiments. C.B performed immunostainings and analysis of RIF1 and MAD2L2. G.O, W.A.B and C.B
254 wrote the manuscript with input from all authors.

255

256 **References**

257

- 258 1. Kline, A. D. *et al.* Diagnosis and management of Cornelia de Lange syndrome: first
259 international consensus statement. *Nature Reviews Genetics* **19**, 649 (2018).
- 260 2. Ansari, M. *et al.* Genetic heterogeneity in Cornelia de Lange syndrome (CdLS) and
261 CdLS-like phenotypes with observed and predicted levels of mosaicism. *Journal of medical*
262 *genetics* **51**, 659–668 (2014).
- 263 3. Castronovo, P. *et al.* Premature chromatid separation is not a useful diagnostic marker
264 for Cornelia de Lange syndrome. *Chromosome Research* **17**, 763–771 (2009).
- 265 4. Mehta, D. *et al.* Characterization of limb differences in children with Cornelia de
266 Lange Syndrome. *American Journal of Medical Genetics Part C: Seminars in Medical*
267 *Genetics* **172**, 155–162 (2016).
- 268 5. Remeseiro, S., Cuadrado, A. & Losada, A. Cohesin in development and disease.
269 *Development* **140**, 3715–3718 (2013).
- 270 6. Dorsett, D. The Drosophila melanogaster Model for Cornelia de Lange Syndrome:
271 Implications for Etiology and Therapeutics. *Am J Med Genet C Semin Med Genet* **172**, 129–
272 137 (2016).
- 273 7. Pastink, A. *et al.* Increased DNA damage sensitivity of Cornelia de Lange syndrome
274 cells: evidence for impaired recombinational repair. *Human Molecular Genetics* **16**, 1478–
275 1487 (2007).
- 276 8. Olley, G. *et al.* BRD4 interacts with NIPBL and BRD4 is mutated in a Cornelia de
277 Lange-like syndrome. *Nature Genetics* (2018). doi:10.1038/s41588-018-0042-y
- 278 9. Di Micco, R. *et al.* Control of embryonic stem cell identity by brd4-dependent
279 transcriptional elongation of super-enhancer-associated pluripotency genes. *Cell Reports* **9**,
280 234–247 (2014).
- 281 10. Lovén, J. *et al.* Selective inhibition of tumor oncogenes by disruption of super-
282 enhancers. *Cell* **153**, 320–334 (2013).
- 283 11. Rahman, S. *et al.* The Brd4 extraterminal domain confers transcription activation
284 independent of pTEFb by recruiting multiple proteins, including NSD3. *Molecular and*
285 *cellular biology* **31**, 2641–2652 (2011).
- 286 12. Jang, M. K. *et al.* The bromodomain protein Brd4 is a positive regulatory component
287 of P-TEFb and stimulates RNA polymerase II-dependent transcription. *Mol. Cell* **19**, 523–
288 534 (2005).
- 289 13. Dev, H. *et al.* Shieldin complex promotes DNA end-joining and counters homologous
290 recombination in BRCA1-null cells. *Nature Cell Biology* **20**, 954–965 (2018).
- 291 14. Ghezraoui, H. *et al.* 53BP1 cooperation with the REV7-shieldin complex underpins

- 292 DNA structure-specific NHEJ. *Nature* **560**, 122–127 (2018).
- 293 15. Gupta, R. *et al.* DNA Repair Network Analysis Reveals Shieldin as a Key Regulator
294 of NHEJ and PARP Inhibitor Sensitivity. *Cell* **173**, 972–988.e23 (2018).
- 295 16. Mirman, Z. *et al.* 53BP1–RIF1–shieldin counteracts DSB resection through CST- and
296 Pol α -dependent fill-in. *Nature* **560**, 112–116 (2018).
- 297 17. Noordermeer, S. M. *et al.* The shieldin complex mediates 53BP1-dependent DNA
298 repair. *Nature* **560**, 117–121 (2018).
- 299 18. Boersma, V. *et al.* MAD2L2 controls DNA repair at telomeres and DNA breaks by
300 inhibiting 5' end resection. *Nature* **521**, 537–540 (2015).
- 301 19. Chapman, J. R. *et al.* RIF1 is essential for 53BP1-dependent nonhomologous end
302 joining and suppression of DNA double-strand break resection. *Mol. Cell* **49**, 858–871
303 (2013).
- 304 20. Feng, L., Fong, K.-W., Wang, J., Wang, W. & Chen, J. RIF1 counteracts BRCA1-
305 mediated end resection during DNA repair. *J. Biol. Chem.* **288**, 11135–11143 (2013).
- 306 21. Di Virgilio, M. *et al.* Rif1 prevents resection of DNA breaks and promotes
307 immunoglobulin class switching. *Science* **339**, 711–715 (2013).
- 308 22. Escribano-Díaz, C. *et al.* A cell cycle-dependent regulatory circuit composed of
309 53BP1-RIF1 and BRCA1-CtIP controls DNA repair pathway choice. *Mol. Cell* **49**, 872–883
310 (2013).
- 311 23. Floyd, S. R. *et al.* The bromodomain protein Brd4 insulates chromatin from DNA
312 damage signalling. *Nature* **498**, 246–250 (2013).
- 313 24. Li, X. *et al.* BRD4 Promotes DNA Repair and Mediates the Formation of Tmprss2-
314 ERG Gene Rearrangements in Prostate Cancer. *Cell reports* **22**, 796–808 (2018).
- 315 25. Wilson, A. J., Stubbs, M., Liu, P., Ruggeri, B. & Khabele, D. The BET inhibitor
316 INCB054329 reduces homologous recombination efficiency and augments PARP inhibitor
317 activity in ovarian cancer. *Gynecologic Oncology* **149**, 575–584 (2018).
- 318 26. Pongas, G. *et al.* BRD4 facilitates DNA damage response and represses
319 CBX5/Heterochromatin protein 1 (HP1). *Oncotarget* **8**, 51402–51415 (2017).
- 320 27. Kastan, M. B. & Bartek, J. Cell-cycle checkpoints and cancer. *Nature* **432**, 316
321 (2004).
- 322 28. Sun, C. *et al.* BRD4 Inhibition Is Synthetic Lethal with PARP Inhibitors through the
323 Induction of Homologous Recombination Deficiency. *Cancer cell* **33**, 401–416.e8 (2018).
- 324 29. Turinetto, V. *et al.* High basal γ H2AX levels sustain self-renewal of mouse
325 embryonic and induced pluripotent stem cells. *Stem Cells* **30**, 1414–1423 (2012).
- 326 30. Panier, S. & Boulton, S. J. Double-strand break repair: 53BP1 comes into focus. *Nat.*
327 *Rev. Mol. Cell Biol.* **15**, 7–18 (2014).
- 328 31. Shrivastav, M., De Haro, L. P. & Nickoloff, J. A. Regulation of DNA double-strand
329 break repair pathway choice. *Cell Res.* **18**, 134–147 (2008).
- 330 32. Tonkin, E. T., Wang, T.-J., Lisgo, S., Bamshad, M. J. & Strachan, T. NIPBL,
331 encoding a homolog of fungal Scc2-type sister chromatid cohesion proteins and fly Nipped-
332 B, is mutated in Cornelia de Lange syndrome. *Nat. Genet.* **36**, 636–641 (2004).
- 333 33. Gillis, L. A. *et al.* NIPBL mutational analysis in 120 individuals with Cornelia de
334 Lange syndrome and evaluation of genotype-phenotype correlations. *Am. J. Hum. Genet.* **75**,
335 610–623 (2004).
- 336 34. Clouaire, T. & Legube, G. DNA double strand break repair pathway choice: a
337 chromatin based decision? *Nucleus (Austin, Tex.)* **6**, 107–113 (2015).
- 338 35. Sun, Y. *et al.* Histone H3 methylation links DNA damage detection to activation of
339 the tumour suppressor Tip60. *Nat. Cell Biol.* **11**, 1376–1382 (2009).
- 340 36. Logan, C. V. *et al.* DNA Polymerase Epsilon Deficiency Causes IMAGE Syndrome
341 with Variable Immunodeficiency. *American journal of human genetics* **103**, 1038–1044

- 342 (2018).
- 343 37. Rosin, N. *et al.* Mutations in XRCC4 cause primary microcephaly, short stature and
344 increased genomic instability. *Hum. Mol. Genet.* **24**, 3708–3717 (2015).
- 345 38. Murray, J. E. *et al.* Mutations in the NHEJ Component XRCC4 Cause Primordial
346 Dwarfism. *Am J Hum Genet* **96**, 412–424 (2015).
- 347 39. O’Driscoll, M., Gennery, A. R., Seidel, J., Concannon, P. & Jeggo, P. A. An overview
348 of three new disorders associated with genetic instability: LIG4 syndrome, RS-SCID and
349 ATR-Seckel syndrome. *DNA Repair (Amst.)* **3**, 1227–1235 (2004).
- 350 40. Dutto, I., Scalera, C. & Prosperi, E. CREBBP and p300 lysine acetyl transferases in
351 the DNA damage response. *Cell. Mol. Life Sci.* **75**, 1325–1338 (2018).
- 352 41. Litwin, I., Pilarczyk, E. & Wysocki, R. The Emerging Role of Cohesin in the DNA
353 Damage Response. *Genes (Basel)* **9**, (2018).
- 354 42. Buonomo, S. B. C., Wu, Y., Ferguson, D. & De Lange, T. Mammalian Rif1
355 contributes to replication stress survival and homology-directed repair. *Journal of Cell*
356 *Biology* (2009). doi:10.1083/jcb.200902039
- 357 43. Pradeepa, M. M. *et al.* Histone H3 globular domain acetylation identifies a new class
358 of enhancers. *Nature genetics* **48**, 681–686 (2016).
- 359 44. Pintacuda, G. *et al.* hnRNPK Recruits PCGF3/5-PRC1 to the Xist RNA B-Repeat to
360 Establish Polycomb-Mediated Chromosomal Silencing. *Molecular Cell* **68**, 955-969.e10
361 (2017).
- 362
- 363

364 **Methods:**

365 **KEY RESOURCES TABLE**

Antibodies	SOURCE	IDENTIFIER
BRD4	Bethyl	Cat# A301-985A-M
53BP1	Novus	Cat# NB100-304
Normal Rabbit IgG	Santa Cruz	Cat# sc-2025
CHK1	Abcam	Cat# ab47574
CHK1-p	Cell signaling technologies	Cat# 2348
Lamin B	Santa Cruz	Cat# sc-374015
MAD2L2	Abcam	Cat# ab180579
RIF1	A kind gift from Sara Buonomo	Rabbit anti-mouse Rif1 serum 1240 ⁴²
RAD51	Calbiochem	Cat# PC130
Goat anti-Rabbit IgG, secondary, Alexa Fluor 488	Invitrogen	Cat# A11034
Donkey anti-Rabbit IgG, secondary, Alexa Fluor 586	Invitrogen	Cat# A10042

366

Primers	Forward	Reverse
ChIP-qPCR		
Sox2 SE	TAGAGGAAGGAGCTGGAG GA	AAGGAAAGAAGGAGGG ACGG
Klf4 SE	CACAATGCCAGCTATGCGA T	TCCTGCCCAAATGTGAG GAT
Nanog SE	GTGAAGGTAGTTTGCTGGG C	GGTCCTTTCCACCCCTC TAC
Oct4 SE	CCTTCGTTCCAGAGCATGGT G	GAGCCTACCCTGAACTT CCC
Expression		
Klf4	GTGCAGCTTGCAGCAGTAA C	AGCGAGTTGGAAAGGA TAAAGTC
Myc	CCCTAGTGCTGCATGAGGA	CGTAGTTGTGCTGGTGA GTG
Oct4	CGAGAACAATGAGAACCTT C	CCTTCTCTAGCCCAAGC TGAT
Nanog	TGGTCCCCACAGTTTGCCT AGTTC	CAGGTCTTCAGAGGAA GGGCGA

367

Deposited Data		
BRD4-WT ChIP-seq	This paper	GSE130659
BRD4-Y430C ChIP-seq	This paper	GSE130659
WT 4sU-seq	This paper	GSE130659
Y430C 4sU-seq	This paper	GSE130659
WT Spike-in RNAseq	This paper	GSE130659
Y430C Spike-in RNAseq	This paper	GSE130659
	This paper	GSE130659

368

369

370

Software and Algorithms		
Bowtie2	Langmead and Salzberg, 2012	http://bowtie-bio.sourceforge.net/bowtie2/index.shtml
MACS2		https://github.com/taoliu/MACS
FACSDiva software	BD Bioscience	
TopHat	Trapnell <i>et al.</i> , 2012	https://ccb.jhu.edu/software/tophat/index.shtml
Cufflinks	Trapnell <i>et al.</i> , 2012	http://cole-trapnell-lab.github.io/cufflinks/
Deeptools2	Ramirez <i>et al.</i> , 2016	http://deeptools.readthedocs.io/en/latest/index.html
SAMtools	Li <i>et al.</i> , 2009	http://samtools.sourceforge.net/

371

372 Cell culture

373 Y430C-BRD4 mutant and corresponding wild-type mouse embryonic stem cells (mESCs) were
 374 generated by CRISPR Cas9 genome editing in 46C mESCs as described previously⁸. NIPBL I1206del
 375 and R2298H lymphoblastoid cell lines (LCLs) were obtained from patients^{32,33}. mESCs were cultured in
 376 GMEM medium (GIBCO; 11710035) supplemented with 10% Fetal Calf Serum (FCS), 5%
 377 penicillin-streptomycin, 1 mM sodium pyruvate (GIBCO; 11360070), 1X non-essential amino
 378 acids (GIBCO; 11140050), 50 µM 2-Mercaptoethanol (GIBCO; 31350010), 2 mM L-glutamine
 379 and 500U/ml Leukaemia Inhibitory Factor (in house). Lymphoblastoid cell lines (LCLs) were

380 grown in RPMI 1640 medium (GIBCO; 11875093) supplemented with 15% FCS and 2 mM L-
381 glutamine. All cells were grown at 37°C in a 5% CO₂ humidified atmosphere.

382 **ChIP-qPCR**

383 Cells were harvested by trypsinising and fixed with 1% formaldehyde (Thermo Fisher; 28906) in media
384 (25°C, 10 min). This reaction was quenched with 0.125 M glycine for 5 min. ChIP-qPCR was performed
385 as described previously⁸ (see table for antibodies). DNA was purified using the QIAquick PCR
386 Purification kit (Qiagen, 28104). Input samples were diluted to 1%, and all samples diluted a further
387 10-fold, in ddH₂O. SYBR-green based qPCR reactions were performed in a final volume of 20 µl
388 containing diluted ChIP DNA, SYBR select master mix (ThermoFisher Scientific; 4472908) and 0.25
389 µM/L of each primer (see table). Concentration of IPs are relative to 1% input.

390

391 **ChIP-seq**

392 ChIP was carried out as above. After purification, DNA was eluted in 20 µl and libraries were
393 prepared for ChIP and input samples as previously described⁴³. Samples were sequenced at BGI
394 (Hong Kong; 50-bp single-end reads) using the HiSeq 4000 system (Illumina). Fastq files were quality
395 controlled using FastQC and mapped to the mm9 genome using Bowtie2 (parameters: default). Sam
396 files were converted to bam files and sorted using SamTools. Homer was used to make tagdirectories
397 (makeTagDirectory, parameters: -unique, fragLength 150) and bedgraphs (makeUCSCfile,
398 parameters: default). For visualisation of BRD4 data, bedgraphs were uploaded to the genome browser
399 UCSC. Peak calling was carried out using MACS2; Duplicates were filtered (filterdup, parameters:--
400 keep-dup=1), peaks called (callpeaks, parameters: -B --nomodel -p 1e-5) and differential peaks were
401 found (bdgdiff, parameters: -g 60 -l 250).

402 deepTools2 was used to make heatmaps; score files were made across specific genomic regions
403 (computeMatrix, parameters: scale-regions scale regions -b 500 -a 500 -bs 50 -bl mm9 blacklist) and
404 these were used to plot heatmaps (plotHeatmap, parameters: --colormap RdBluYl reverse).

405 **JQ1 treatment**

406 1 mM BRD4 inhibitor JQ1+, or its inactive form JQ1- (Merck; 500586) (diluted in DMSO), were added
407 to mESC media at a final concentration of 300 nM. JQ1+/- WT and Y430C mESCs were incubated at
408 37°C with JQ1+/- supplemented media for 48 hrs. Total RNA was extracted from cells using the RNeasy
409 Plus Mini Kit (Qiagen; 74134) and 1 µg RNA was used for cDNA synthesis with SuperScript II Reverse
410 Transcriptase (ThermoFisher Scientific; 18064-014) as per manufacturer's instructions. cDNA was
411 diluted 1:500 for qPCR analysis. qPCR reactions were performed as above (see table for primers).
412 Concentration of JQ1+ cDNA was calculated relative to JQ1- (arbitrarily set to 1).

413 **RT-PCR**

414 RNA was extracted from cells using the RNeasy Mini Kit (Qiagen; 74104) using spin technology, with
415 an additional on-column DNA digestion using the RNase-Free DNase Set (Qiagen; 79254). cDNA was
416 synthesised from 1 µg RNA using SuperScript II Reverse Transcriptase (ThermoFisher Scientific;

417 18064-014) as per manufacturer's instructions. cDNA was diluted 1 in 25 for qPCR analysis. SYBR-
418 green based qPCR reactions were performed in a final volume of 20 μ l containing diluted cDNA, SYBR
419 select master mix (ThermoFisher Scientific; 4472908) and 0.5 μ M/l of region specific intron-spanning
420 primer pairs.

421 **4sU-seq**

422 4sU RNA was generated and isolated as described previously⁴⁴, with the following changes: cells
423 were incubated at 37°C with 4sU-supplemented medium for 20 min. The reaction was incubated with
424 Biotin-HPDP with rotation for 1.5 hours at RT. For recovery of biotinylated 4sU-RNA, 1 μ l of streptavidin
425 beads was added per μ g of RNA. Columns were washed using 900 μ l washing buffer and RNA was
426 eluted by 2 sequential additions of 100 μ l Elution Buffer (100 mM DTT) to the column and eluates
427 combined. RNA was further purified using the RNAeasy MinElute Clean-up kit (Qiagen; 74204)
428 according to the manufacturer's guidelines, eluting in 20 μ l water. 1 μ l of 4sU-labeled RNA was quality-
429 checked by running on a 2100 Bioanalyzer Instrument (Agilent).

430 To make 4sU sequencing libraries, 4sU labelled RNA was first depleted of rRNA using the Low Input
431 Ribominus Eukaryotic System V2 (ThermoFisher Scientific; A15027) as per the manufacturer's
432 instructions. 600 ng of 4sU labelled RNA was used as input, and eluted in 5 μ l RNase free water. All of
433 the resulting rRNA free RNA was used to prepare 4sU sequencing libraries, using NEBnext Ultra
434 Directional RNA library prep kit of Illumina (NEB; E7420). RNA fragmentation was carried out at 94°C
435 for 15 min, as suggested for intact RNA. Libraries were indexed with Multiplex Oligos for
436 Illumina® (Index Primers Set 1) (NEBnext; E7335) and amplified by PCR for 13 cycles. Library
437 concentration and correct size distribution was confirmed on the Agilent 2100 Bioanalyser with the DNA
438 HS Kit. Libraries were sequenced at BGI (Hong Kong; 100-base paired-end reads) using the HiSeq
439 4000 system (Illumina).

440 Fastq files were quality controlled using FastQC and mapped to the mm9 genome using tophat
441 (parameters: --library-type fr-firststrand -r 200). Homer was used to make tagdirectories
442 (makeTagDirectory, parameters: -unique -sspe -flip -fragLength 150), and to make bedgraphs for
443 visualisation on UCSC (makeUCSCfile, parameters: -strand separate -style rnaseq). Cufflinks was used
444 for peak calling; transcripts were assembled for individual experiments (cufflinks, parameters: -m 200
445 --library-type fr) and both replicates of WT and Y430C were combined to form one assembly (cuffmerge,
446 parameters: default). Differentially expressed peaks were determined from this assembly using cuffdiff
447 (Cuffdiff. Parameters: default).

448 Heatmaps were generated as above.

449 **Spike-in RNA-seq**

450 S2 cells were cultured in Schneider's Drosophila Medium (Invitrogen; 11720-034), supplemented with
451 10% heat-inactivated FCS and 5% penicillin-streptomycin. Cells were passaged once they reached a
452 density of $\sim 2 \times 10^7$ cells/ml and seeded at a density of $\sim 4 \times 10^6$. Cells were grown at 28°C in a 5% CO₂
453 humidified atmosphere. Cells were frozen at a density of $\sim 1 \times 10^7$ cells/ml in 45% conditioned

454 Schneider's Drosophila Medium media (containing 10% FCS), 45% fresh Schneider's Drosophila
455 Medium supplemented with 10% FCS, and 10% DMSO, and stored in liquid nitrogen.

456 mESCs and S2 cells were harvested and counted. 0.2 million S2 cells were mixed with 10 million
457 mESCs, and RNA was extracted using the RNeasy Mini Kit (Qiagen; 74104) using spin technology,
458 with an additional on-column DNA digestion using the RNase-Free DNase Set (Qiagen; 79254). RNA
459 was depleted of rRNA and RNA-seq libraries prepared as for the 4sU-seq.

460 **Growth assay**

461 WT and Y430C mESCs were each seeded in 4 wells of a 6 well plate (1×10^4 cells/well). WT and Y430C
462 cells from 1 well were trypsinised and counted at 24, 48, 72 and 96 hrs post seeding. Counting was
463 carried out manually using a haemocytometer. The addition of trypan blue dye allowed for the exclusion
464 of dead cells.

465 **Flow cytometry**

466 2 million mESCs were fixed in 70% ethanol (in PBS) at 4°C for 1 hr. Fixed cells were centrifuged at
467 2000 rpm at 4°C for 5 min, washed twice with PBS and resuspended in 500 μ l PBS. 20 μ g RNase A
468 was added and cells were incubated at 37°C for 10 min. Cells were stained with propidium iodide at a
469 final concentration of 50 μ g/ml. Acquisition was carried out on a BD LSRFortessa cell analyser,
470 collecting 25,000 events per sample. Results were analysed using BD FACSDiva 8.0.1 and gated cells
471 were manually categorized into cell cycle stages G0/G1, S and G2/M.

472 **NCS treatment and CHK-1 protein western blots**

473 Cells were incubated with mESC media supplemented with neocarzinostatin (Sigma; N9162) (NCS), to
474 a final concentration of 25 ng/ml, for 15 min at 37°C. Cells were then washed with PBS and fresh, non-
475 supplemented media was added. Protein was either extracted straight away, or after incubation at 37°C
476 for varying lengths of time. Ice-cold RIPA buffer (150 mM sodium chloride; 1.0% NP-40; 0.5% sodium
477 deoxycholate; 0.1% SDS; 50 mM Tris, pH 8.0) was added to plates (1 ml per 10^7 cells) and cells were
478 scraped and transferred into pre-chilled microcentrifuge tubes. Tubes were shaken at 4°C for 30 min
479 before centrifugation at 20,000 x g for 15 min. Supernatant was retained and quantified. For western
480 blot analysis, equal amounts of protein were boiled in 1X NuPage LDS buffer (ThermoFisher Scientific,
481 NP0008) with 1X NuPage reducing agent (ThermoFisher Scientific; NP0004) for 5 min and separated
482 on a 3-8% tris-acetate gel (ThermoFisher Scientific; EA0375BOX). Following electrophoresis, proteins
483 were transferred to nitrocellulose membranes (ThermoFisher Scientific) and immunoblotted with
484 primary antibodies overnight at 4°C. Membranes were washed 3 X TBST and probed with HRP-
485 conjugated secondary antibody for 1 hr at RT. After 3 more washes in TBST, membranes were
486 incubated with SuperSignal™ West Femto Maximum Sensitivity Substrate (ThermoFisher
487 Scientific; 34095) for 5 min and imaged using ImageQuant™ LAS 4000 (GE Healthcare).

488

489 **Immunofluorescence**

490 mESCs for immunofluorescence experiments were cultured on gelatinised coverslips and LCLs were
491 grown in suspension. LCLs were harvested and resuspended in PBS to 1.8×10^5 cells/ml. 500 μ l of cell
492 suspension was added to a Shandon™ Single Cytotunnel™ (ThermoFisher Scientific; 5991040), with a microscope slide attached. Slides were centrifuged at 800 rpm for 5 min, after which
493 the LCLs had attached to the slide. All cells were fixed in 4% paraformaldehyde for 10 min and washed
494 3X 3 min in PBS. Cells were then permeabilised in 0.5% Triton in PBS for 10 min and washed 3X 3 min
495 in PBS. Cells were blocked in 1% BSA in PBS for 30 min at RT, incubated with primary antibody diluted
496 in 1% BSA for 1 hr at RT and washed 3X 3 min in PBS. Cells were next incubated with secondary
497 antibody (see table) diluted in 1% BSA for 45 min at RT, washed 3X 3 min in PBS, incubated with DAPI
498 in PBS (250 ng/ml) for 2 min, and washed 3x 3 min in PBS. Coverslips were mounted on slides in
500 Vectashield (Vector; H1000) mounting medium for fluorescence.

501 All slides were viewed, and foci counted, using epifluorescence microscopes. Images were taken using
502 confocal microscopy.

503

504

505

506

507

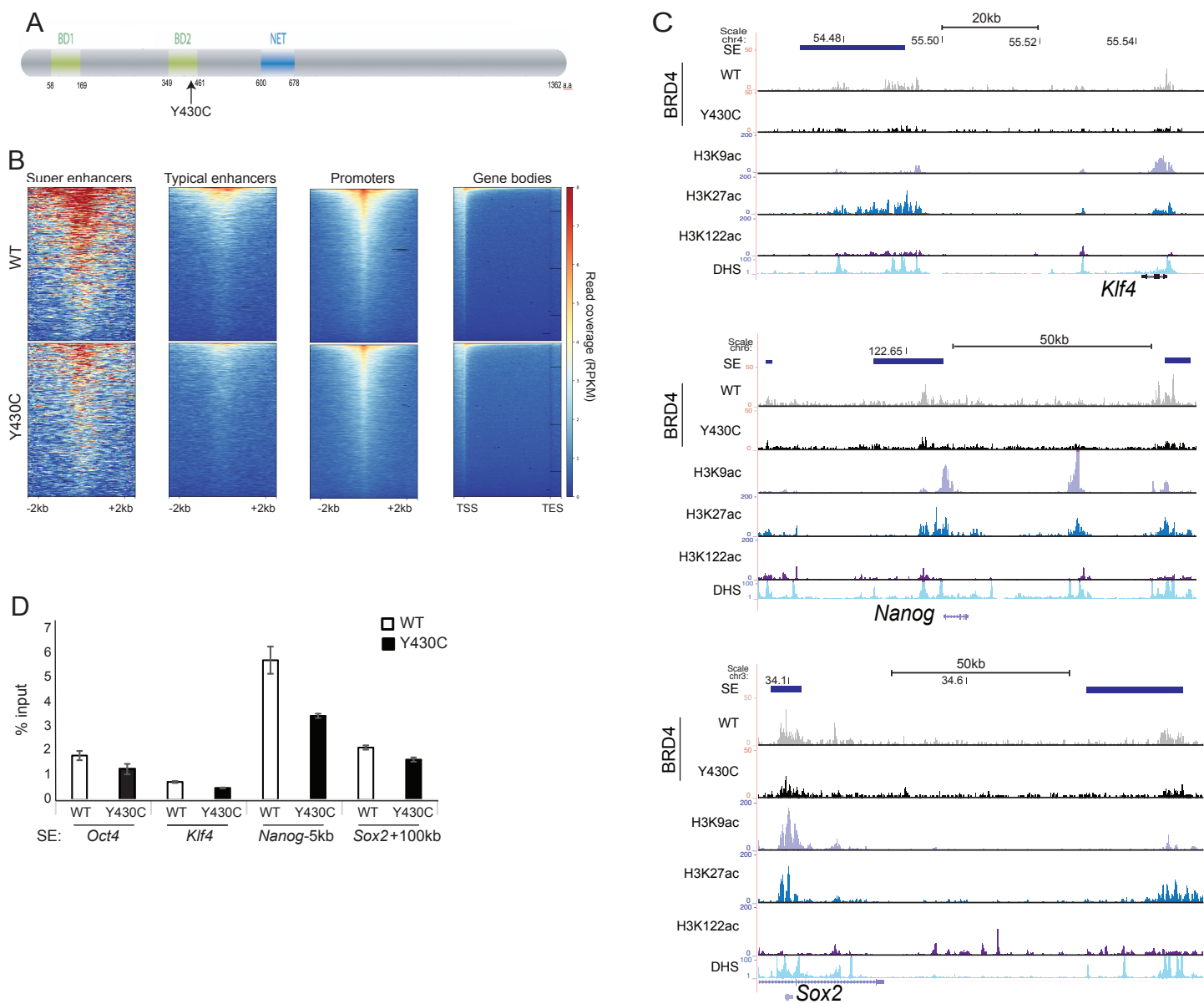


Figure 1. Decreased binding of BRD4 at CREs in Y430C mESCs. A) Cartoon of BRD4 showing location of the Y430C mutation in the second bromodomain (BD2). B) Heatmaps show enrichment of wild-type (WT) and Y430C BRD4 ChIP over super enhancers (SE), typical enhancers, promoters and gene bodies. C) UCSC genome browser screenshot showing reads per 10 million over the *Klf4*, extended *Nanog* and *Sox2* loci for BRD4 ChIP-seq in wild-type (WT) and BRD4^{Y430C} mESCs. Extent of SEs are shown in blue. Below are shown previously published ChIP-seq data for H3K27ac (ENCSR000CDE), H3K9ac (ENCSR000CGS), H3K122ac (GSE66023) and DNase I hypersensitivity (DHS). Genome co-ordinates (Mb) are from the mm9 assembly of the mouse genome. Biological replicate in Supplementary figure 1. D) ChIP-qPCR measuring concentration of BRD4 ChIP DNA relative to input across the SEs of *Oct4*, *Klf4*, *Nanog*, and *Sox2*; in WT and BRD4^{Y430C} mESCs. Data are represented as mean +/- SEM from 3 technical replicates.

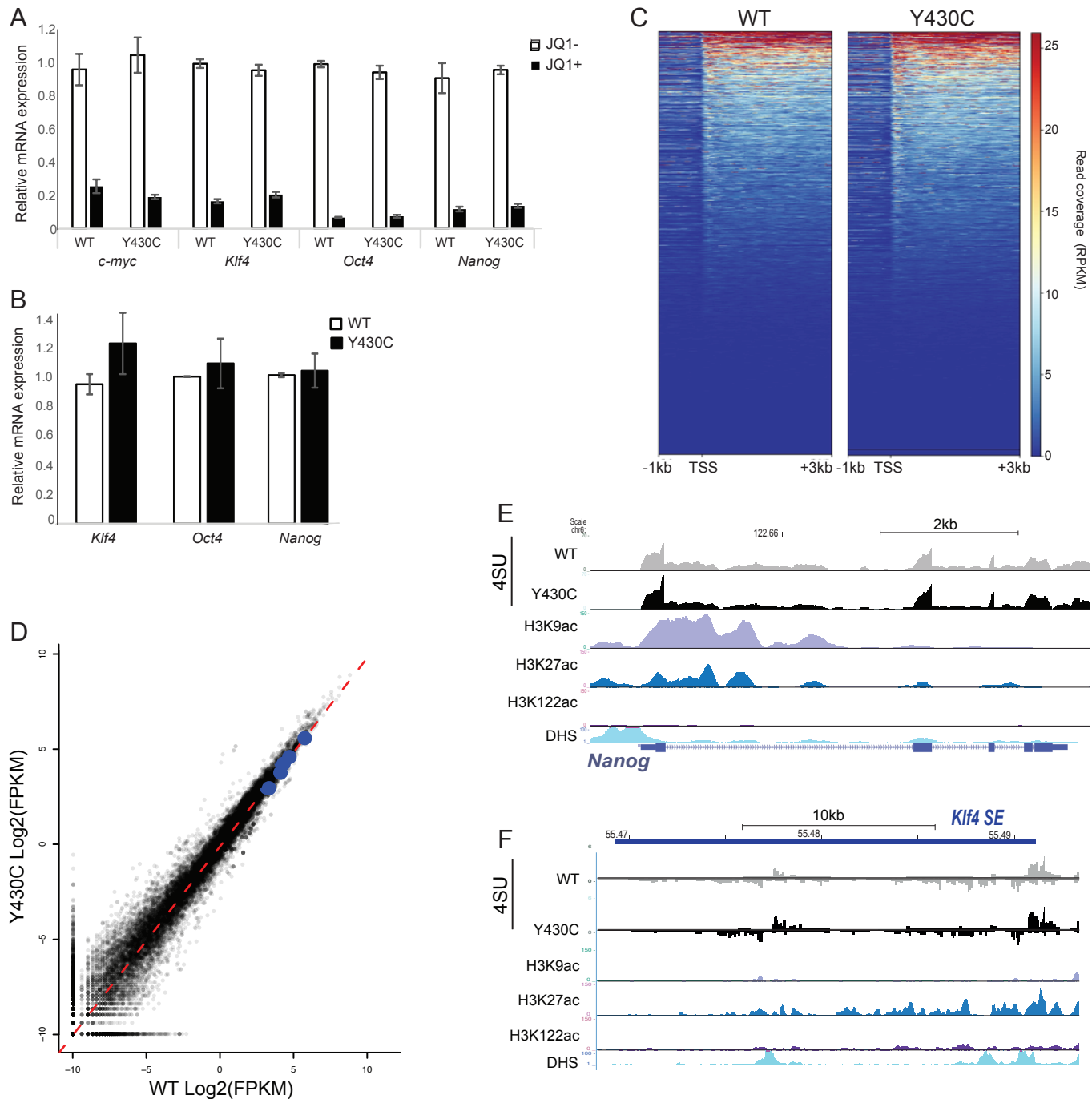


Figure 2. Similar transcription in WT and Y430C mESCs. A) RT-qPCR measuring mRNA of *c-myc*, *Klf4*, *Oct4* and *Nanog* in mESCs after treatment with 300 nM JQ1+, relative to that in untreated cells (JQ1-). Data are represented as mean +/- SEM from 3 technical replicates. B) RT-qPCR measuring mRNA for *Klf4*, *Oct4* and *Nanog* in WT and *BRD4*^{Y430C} mESCs. mRNA concentration is shown relative to WT set at 1. Data are represented as mean +/- SEM from 3 biological replicates. C) Heatmaps show enrichment of 4sU-seq in WT and *BRD4*^{Y430C} cells over transcribed regions (-1kb, TSS and +3kb) (mm9_refseq). D) Scatter plot of the 4sU-seq data in WT and Y430C cells, highlighting pluripotency genes in blue (*Nanog*, *Sox2*, *Klf4*, *Esrrb*, *Pou5f1*). Red dashed line shows best fitted line. Pearson correlation coefficient=0.98. E and F) UCSC browser screenshot showing 4sU-seq reads per 10 million over (E) the *Nanog* locus and (F) the *Klf* super-enhancer in WT and *BRD4*^{Y430C} mESCs and ChIP-seq tracks for various histone modifications and DNase I hypersensitivity in WT cells. Genome co-ordinates (Mb) are from the mm9 assembly of the mouse genome. Data from a biological replicate in Supplementary figure 2.

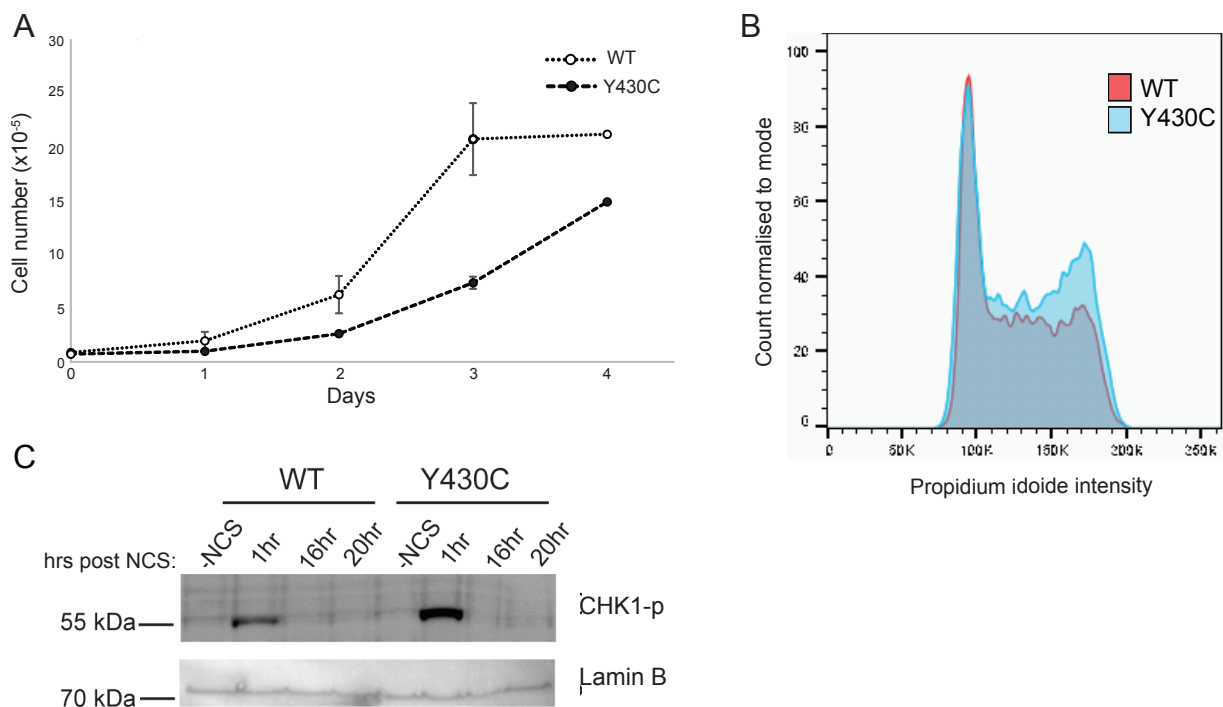


Figure 3. Increased G2/M checkpoint activation in Y430C mESCs. A) Graph shows average number of WT and *BRD4*^{Y430C} cells per well at 1, 2, 3 and 4 days post seeding. Data are represented as mean \pm SEM from 3 technical replicates. B) Overlaid graphs show WT and *BRD4*^{Y430C} cell cycle profiles, as determined by flow cytometry. Graphs illustrate the cell count, which correlates to propidium iodide intensity. Biological replicate in Supplementary Figure 3A. C) Immunoblot using antibodies against CHK1-p and Lamin B after treatment of WT and *BRD4*^{Y430C} mESCs with NCS and for various times (hrs) of recovery.

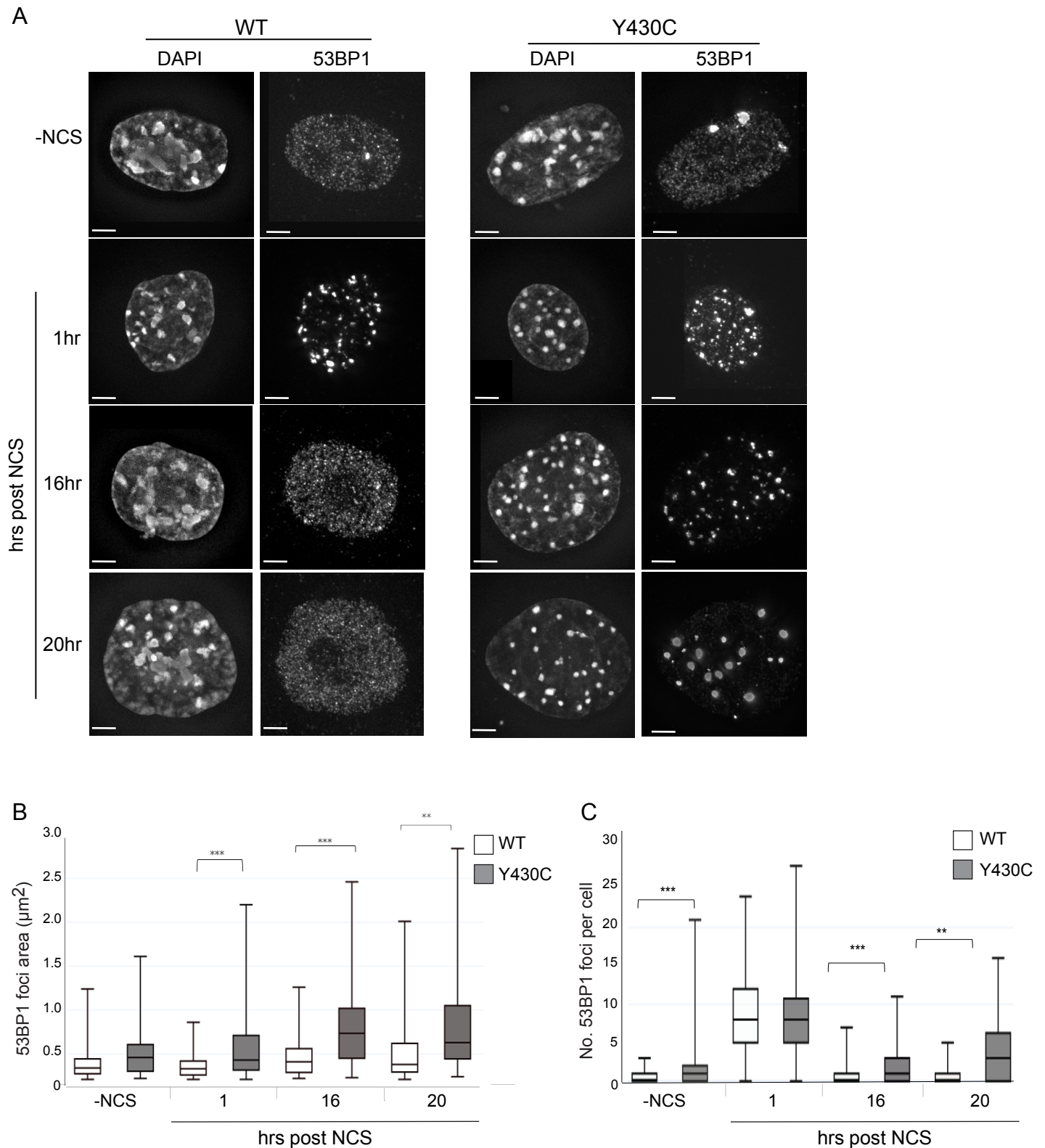
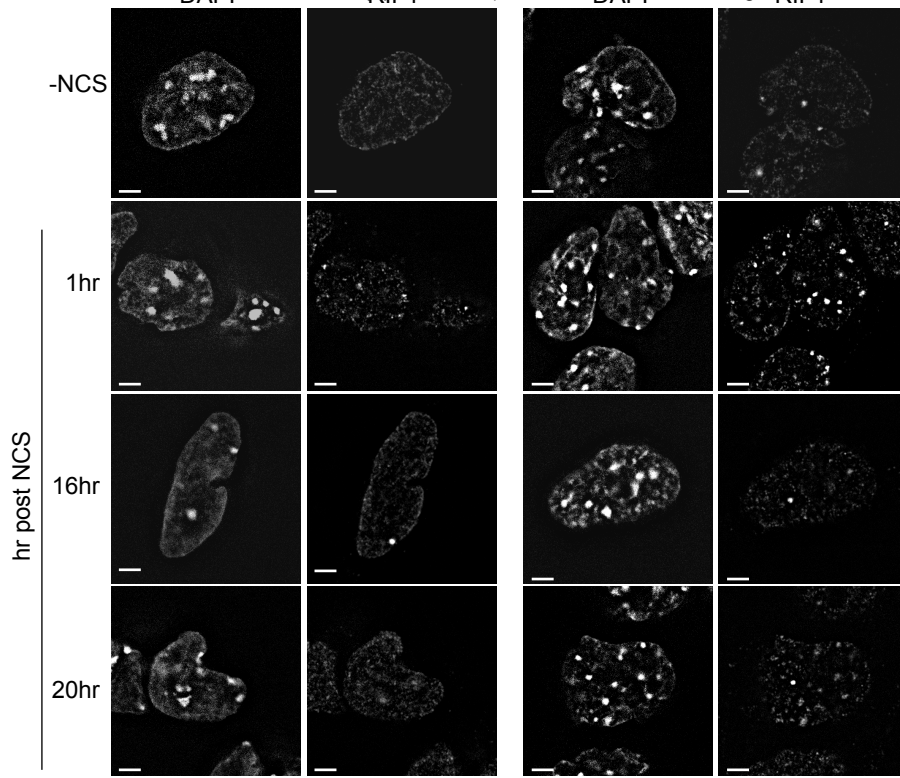


Figure 4. Increased size and number of 53BP1 foci after DSB induction in Y430C mESCs.

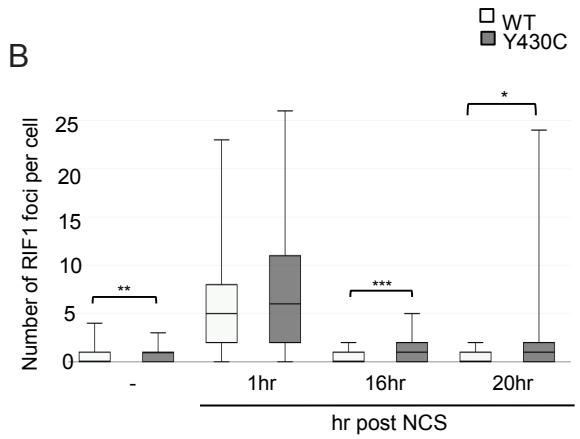
A) Immunofluorescence for 53BP1 in the DAPI-stained nuclei of wild-type and *BRD4*^{Y430C} mESCs upon treatment with NCS and after recovery periods up to 20 hrs. B&C) Box-plots show area (µm²) and number of 53BP1 foci per cell, respectively, in WT and *BRD4*^{Y430C} cells after treatment with NCS in one representative experiment. Horizontal lines within boxes show medians, boxes are inter-quartile ranges and whiskers are range. P-values were calculated with Mann-Whitney U test. * < 0.05, ** < 0.01, *** < 0.001.

A

WT Y430C
DAPI RIF1 DAPI RIF1

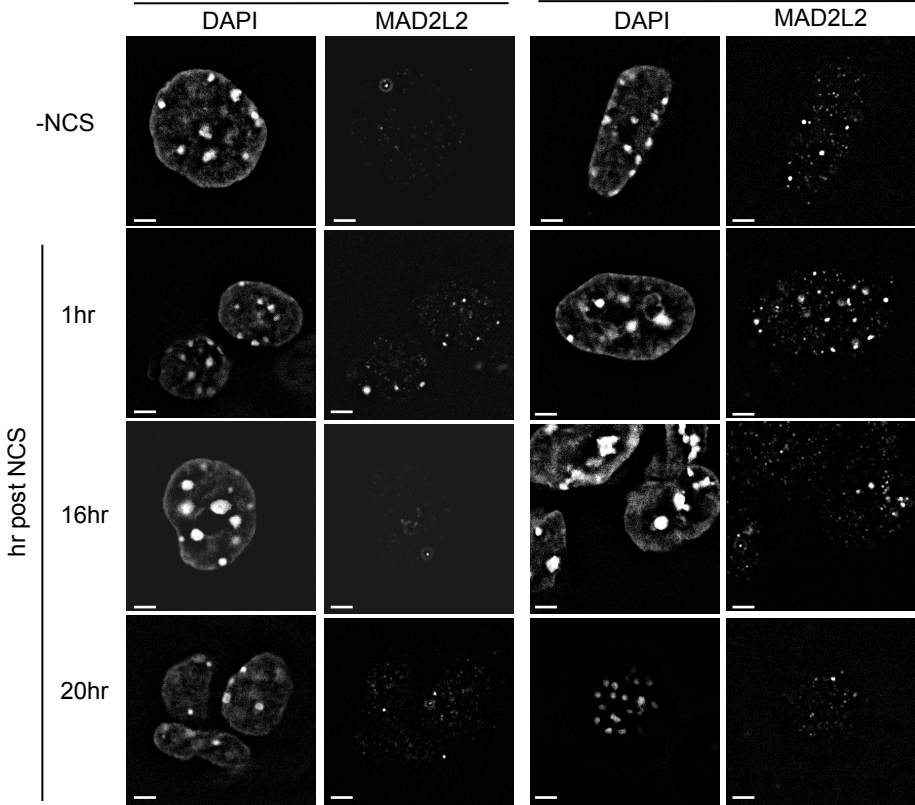


B



C

WT Y430C
DAPI MAD2L2 DAPI MAD2L2



D

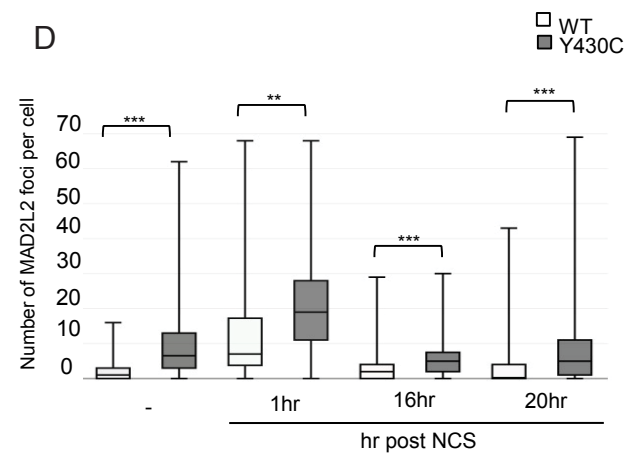


Figure 5. Increased RIF1 and MAD2L2 foci after DSB induction in Y430C mESCs. A) Representative images of wild-type and Y430C mESCs upon RIF1 immunofluorescence and DAPI staining after treatment with NCS. B) Box-plot shows number of RIF1 foci per cell, respectively, in WT and Y430C cells after treatment with NCS in one representative experiment. Horizontal lines within boxes show medians, boxes are inter-quartile ranges and whiskers are range. P-values were calculated with Mann-Whitney U test. * < 0.05, ** < 0.01, *** < 0.001. C) Representative images of wild-type and Y430C mESCs upon MAD2L2 immunofluorescence and DAPI staining after treatment with NCS. D) Box-plot shows number of MAD2L2 foci per cell, respectively, in WT and Y430C cells after treatment with NCS in one representative experiment. Horizontal lines within boxes show medians, boxes are inter-quartile ranges and whiskers are range. P-values were calculated with Mann-Whitney U test. * < 0.05, ** < 0.01, *** < 0.001.

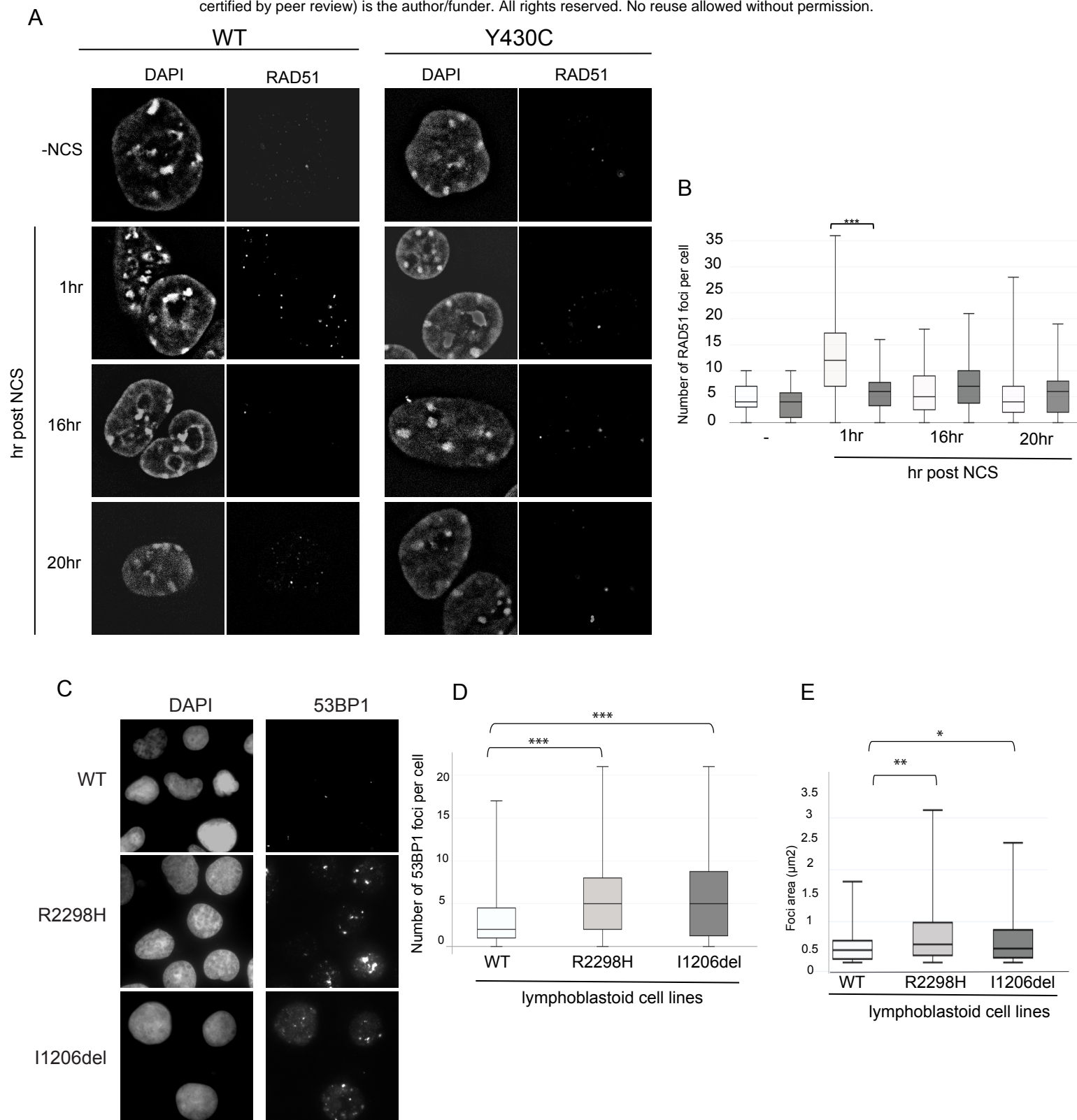


Figure 6. Evidence for DNA repair defects in CDLS A) Representative images of wild-type and Y430C mESCs upon RAD51 immunofluorescence and DAPI staining after treatment with NCS. B) Box-plot shows number of RAD51 foci per cell, respectively, in WT and Y430C cells after treatment with NCS in one representative experiment. Horizontal lines within boxes show medians, boxes are inter-quartile ranges and whiskers are range. P-values were calculated with Mann-Whitney U test. * < 0.05, ** < 0.01, *** < 0.001. C) Representative images of wild-type, R2298 and I1206del LCLs upon 53BP1 and DAPI immunofluorescence. D&E) Box-plots show number of 53BP1 foci per cell and area of 53BP1 foci (μm^2), respectively, in WT, R2298H and I1206del LCLs in one representative experiment. Horizontal lines within boxes show medians, boxes are inter-quartile ranges and whiskers are range. P-values were calculated with Mann-Whitney U test. * < 0.05, ** < 0.01, *** < 0.001.